Materials Advances

ROYAL SOCIETY OF CHEMISTRY

PAPER

View Article Online
View Journal | View Issue

Cite this: *Mater. Adv.*, 2022, 3, 5406

Density effects of vertical graphene nanowalls on supercapacitor performance

Hongtao Sui, *[a] Nguyen Van Toan[b] and Takahito Ono*[ab]

Vertical graphene (VG) nanowalls formed with controllable densities by adjusting $CH_4:H_2$ flow ratios are achieved on silicon wafer substrates *via* plasma-enhanced chemical vapor deposition. The pseudocapacitive materials of MnO_2 enhancing the energy storage capability are electrodeposited on VG nanowalls. The VG densities of 0.83 mg cm^{-2}, 2.35 mg cm^{-2}, and 3.63 mg cm^{-2} fabricated with the $CH_4:H_2$ flow ratios of 1 : 5, 1 : 2.5, and 1 : 1 are carefully controlled. The supercapacitor electrode formed with a flow ratio of 1 : 2.5 exhibits the highest specific capacitance of 166 mF cm^{-2} at a current density of 0.5 mA cm^{-2} among the three electrodes. Furthermore, an asymmetric supercapacitor device with MnO_2/VG/Si as the positive electrode and carbon black as the negative electrode is assembled. The supercapacitor device exhibits excellent electrochemical performance with a specific capacitance of 230.9 mF cm^{-2}, a maximum energy density of 103.9 μW h cm^{-2}, and the largest power density of 4.5 mW cm^{-2}. This study presents the essential insights into the density effects on pseudocapacitive supercapacitor electrodes and the promising methods to prepare energy-storage devices with high electrochemical performance.

Received 24th January 2022,
Accepted 17th May 2022

DOI: 10.1039/d2ma00074a

rsc.li/materials-advances

1. Introduction

The rapid development of portable and electronic devices, including an integrated circuit and a micro-electromechanical system, requires readily accessible electrical power sources and demands energy storage systems with low cost, high energy and power density, and excellent cycling performance.[1,2] Among numerous energy storage devices, supercapacitors are considered to be suitable power sources to fulfill the demands for the modern world due to their elevated energy density, excellent rate capability and long cycling life.[3] Graphene nanowalls, with the characteristics of high electrical conductivity, high surface area and two-dimensional structures, are promising and appropriate scaffolds to construct supercapacitor electrodes.[4–6] Meanwhile, pseudocapacitive materials, such as MnO_2, ZnO, RuO_2, and PANI, are being explored to improve the electrochemical performance for supercapacitors, which show excellent energy storage capability compared to EDLCs due to the energy-storage mechanism involving a faradaic redox reaction.[7,8] Among those materials, MnO_2 is considered to be one of the suitable transition metal oxides comprising supercapacitor electrodes because of the low cost, environmental friendliness, and high intrinsic capacitance (1370 F g^{-1}).[4,9–13] Meanwhile, the supercapacitor electrodes based on metal–MnO_2 materials exhibit excellent electrochemical performance compared to MnO_2-based pseudocapacitive materials.[14–16] However, the poor electrical conductivity of MnO_2 results in slow ion transfer rates and a surface redox reaction containing a very thin layer involved in the charge–discharge procedure, limiting the utilization of MnO_2-based supercapacitor electrodes.[17–19] Therefore, the MnO_2/graphene composites have been widely investigated as the most promising candidates for supercapacitor electrodes. For example, a graphene oxide/MnO_2/Ni foam composite *via* a mild fabrication method with a specific capacitance of 288 F g^{-1} at a current density of 0.5 A g^{-1} has been synthesized.[20] The MnO_2/graphene fabricated using a one-step hydrothermal synthesis exhibits a specific capacitance of 255 F g^{-1} at 0.5 A g^{-1} with a capacitance retention of 84.5% after 10 000 cycles.[21] The needle-like structure of MnO_2 coated on GO is formed, showing improved performance compared with the other structures of MnO_2.[22] An exfoliated graphene paper deposited by MnO_2 nanoflowers with a specific capacitance of 385.2 F g^{-1} at 1 mV s^{-1} is reported. Meanwhile, the supercapacitor device with graphene paper/MnO_2 as the positive electrode and graphene as the negative electrode is assembled, showing an area-normalized specific capacitance of 76.8 mF cm^{-2} at 0.05 mA cm^{-2} and a capacitance retention of 82.2% after 5000 cycles.[23] The MnO_2/graphene composites with the freestanding structures require the current collectors (*e.g.*, Ni foam or PET) and binders

[a] *Micro System Integration Center, Tohoku University, Sendai 980-8579, Japan. E-mail: hongtao.sui.a4@tohoku.ac.jp, takahito.ono.d4@tohoku.ac.jp; Tel: +81-22-795-5810*
[b] *Department of Mechanical Systems Engineering, Tohoku University, Sendai 980-8579, Japan*

(*e.g.*, PVDF) to enhance the robustness of the fabricated electrodes. However, the aggregation of graphene materials jeopardizes the electrochemical performance of supercapacitor electrodes.[24–26] More importantly, the poor controllability over the microstructures of the graphene scaffolds supporting and dispersing the active pseudocapacitive materials increases the difficulty of investigating the morphology and density effects on the performance of supercapacitor electrodes. The vertical graphene nanowalls deposited directly on substrates, followed by the coatings of pseudocapacitive materials, have been synthesized as supercapacitor electrodes with the highly controllable microstructures and well-dispersed nanowalls.[5,27–33] Yu *et al.* have reported that the vertical graphene-based supercapacitor electrodes show a superior performance compared with lateral graphene structures.[34] The VG nanowalls can be formed with a highly tunable morphology and density, which provides access to investigate the modifiable scaffolds influencing the performance of supercapacitor electrodes. Nevertheless, the density effects of graphene scaffolds on the electrochemical performance of supercapacitor electrodes have not been systematically studied. To investigate the density effects of scaffolds, the deposition of pseudocapacitive materials with highly distributed structures on vertical graphene nanowalls by using water–ethanol solvents to prepare electrolytes, instead of depositing pseudocapacitive materials on the top sides of vertical graphene using water-based electrolytes, have been made in our previous work.[33]

In this work, the vertical graphene nanowalls with controllable densities by adjusting the flow ratios of $CH_4:H_2$ are fabricated on silicon wafer substrates as supercapacitor electrodes *via* plasma-enhanced chemical vapor deposition (PECVD), followed by the electrochemical deposition of MnO_2 under a constant condition. The silicon wafers are applied as the substrates with the advantages of (1) the ideally flat surface with easily observed status eliminates the roughness effects on the growth of VG; (2) the natural SiO_2 nano-layers on the surface of silicon wafers enhance the bonding intensity of VG with substrates; (3) the MnO_2/VG/Si constructions provide a novel approach for the widespread applications in the electronic and semiconductor fields.[33] Although the manganese dioxide possesses a lower theoretical specific capacitance among the other types of metal oxides, such as RuO_2 (1400–2000 F g^{-1}), and Co_3O_4 (3560 F g^{-1}), it has tunable microstructures and higher potential windows ($\sim$1 V) than those of RuO_2 and Co_3O_4.[19,33,35,36] The improved distributions of MnO_2 depositions achieved by using a mixture of ethanol and distilled water as the solvent facilitate the dispersion of MnO_2 on VG nanowalls, which clearly reveal the density effects of VG scaffolds. The supercapacitor electrode with the medium-density of VG nanowalls shows the largest area-normalized specific capacitance among all the electrodes. Subsequently, the asymmetric supercapacitor device with MnO_2/VG/Si as the positive electrode and carbon black as the negative electrode is assembled. The carbon black nanoparticles with a diameter of $\sim$30 nm possess the advantages of (1) high electric conductivity, (2) high surface area, and (3) nanostructures corresponding to the positive electrodes with VG nanowalls. The device demonstrates a greatly superior electrochemical performance and has strong potential for the applications powering microsensors or electronics.

2. Experimental method

2.1 Preparation of electrodes consisting of VG and MnO_2 on silicon wafer substrates

The VG nanowalls with tunable densities were deposited *via* microwave plasma-enhanced chemical vapor deposition (MPECVD, Seki-AX5200S) on silicon wafer substrates by adjusting the flow ratios of $CH_4:H_2$. Briefly, the silicon wafers were loaded into the deposition chamber vacuumed for 7 hours before the deposition procedure. Then, the gas of H_2 was introduced into the chamber under the plasma power at 650 W, increasing the pressure to 6000 Pa. Subsequently, the gas of CH_4 as the carbon source with the flow rate of 20 sccm was injected into the growing chamber to initiate the VG growth for 30 min. The flow rates of H_2 were set to 20 sccm, 50 sccm, and 100 sccm, corresponding to the $CH_4:H_2$ ratios of 1 : 1, 1 : 2.5, and 1 : 5 with the identification of $VG_{1:1}$, $VG_{1:2.5}$, and $VG_{1:5}$, respectively. Furthermore, the pseudocapacitive materials of MnO_2 were electrodeposited on VG nanowalls by using a three-electrode system with the as-prepared VG, platinum foil, and Ag/AgCl as the working, counter, and reference electrodes. The electrodeposition was conducted under a constant voltage of 0.6 V for 400 s in all the as-prepared VGs by using the electrolyte containing 0.1 M of Mn $(CHCOO)_2$ and 0.1 M of Na_2SO_4 dissolved in the mixture of ethanol and distilled water (ratio 2 : 3). The MnO_2-coated VGs were then named $MnO_2/VG_{1:1}$, $MnO_2/VG_{1:2.5}$, and $MnO_2/VG_{1:5}$.

2.2 Characterization

The microstructures and morphologies of VGs and MnO_2-coated VG composites were investigated using scanning electron microscopy (Hitachi SU70, FE-SEM). The powders scratched from the MnO_2/VG-deposited silicon wafer substrates, dispersed in ethanol, and dropped onto copper grids, were observed using transmission electron microscopy (TEM, JEOL JEM-2100F). The chemical compositions and structures were analyzed by X-ray photoelectron spectroscopy (XPS).

The electrochemical measurements with the three-electrode system in a typical aqueous solution of 1 M Na_2SO_4 for a single electrode and two-electrode system for a full device were conducted by using an electrochemical workstation (HZ-7000, Hokuto). The MnO_2/VG, platinum, and Ag/AgCl were used as working, counter, and reference electrodes in the three-electrode system. The evaluations of a single electrode under the working potential window of 0–1 V and the full cell in the potential range of 0–1.8 V were performed employing cyclic voltammetry (CV) and galvanostatic (GV) charge–discharge curves. The CV tests were carried out under the typical scan rates varying from 5 mV s^{-1} to 100 mV s^{-1}. The GV curves were obtained with current densities between 0.5 mA cm^{-2} and

5 mA cm^{-2}. Finally, electrochemical impedance spectroscopy (EIS) (ALS Model 7082E) was conducted in a frequency between 0.1 Hz and 500 kHz with the sinusoid potential of 5 mV for a single electrode and full cell.

3. Results and discussion

3.1 SEM and TEM of VG and MnO_2-coated VG

The tunable density of vertical graphene adjusted by the operation parameters, such as gas flow rates, chamber pressure, temperature, *etc.*, has been obtained in the previous literature.[37–40] As shown in Fig. 1(a)–(c), the SEM images exhibit the surface morphologies of the as-deposited VG nanowalls, corresponding to $VG_{1:1}$, $VG_{1:2.5}$, and $VG_{1:5}$, respectively. The uniform distributions with the decreasing density of the nanosheets can be observed when the CH_4 concentration decreases from 50 at% to 16.67 at%, suggesting the good and controllable growth of VG nanowalls. The translucent nanosheets, observed under the acceleration voltage of an electron beam (10 kV), with the similar thickness in all VG depositions indicate the ultra-thin nanowalls and homogenous thickness on the whole layers, which agrees with the previous reports that increasing concentration of CH_4 leads to the higher nucleation tendency generating the higher density of VG nanowalls with the constant thickness of nanosheets.[37,41,42] Furthermore, the BET and BJH measurements were conducted to demonstrate the surface area and average pore size. The surface area values of $VG_{1:1}$, $VG_{1:2.5}$, and $VG_{1:5}$ are 40.93 m^2 g^{-1}, 27.12 m^2 g^{-1}, and 21.61 m^2 g^{-1}, respectively. The decreases of surface area, with the decreasing amounts of deposited VG, correspond to the reducing densities from $VG_{1:1}$ to $VG_{1:5}$. The BJH results with the values of 12.59 nm, 19.58 nm, and 35.05 nm for $VG_{1:1}$, $VG_{1:2.5}$ and $VG_{1:5}$, agree with the changes from denser microstructures for $VG_{1:1}$ to a sparser morphology for $VG_{1:5}$. A more detailed information on the characterization of VG nanowalls can be found in our previous work.[33] Fig. 1(a′)–(c′) show the surface morphologies of MnO_2-coated VGs formed *via* electrochemical deposition on $VG_{1:1}$, $VG_{1:2.5}$, and $VG_{1:5}$ under the same conditions under the deposition potential of 0.6 V for 400 s. The homogeneous distributions of MnO_2-coated nanowalls with a larger thickness of around 600 nm in MnO_2/$VG_{1:1}$ (Fig. 1(a′)) and a smaller thickness of approximately 400 nm in $MnO_2/VG_{1:2.5}$ and $MnO_2/VG_{1:5}$ (Fig. 1(b′) and (c′)) suggest the uniform growth of MnO_2 on the surface of nanowalls. The identical thicknesses of MnO_2-coated nanowalls in $MnO_2/VG_{1:2.5}$ and $MnO_2/VG_{1:5}$ indicate the same deposition rate on each nanowalls. As shown in the BET results, the higher density of VG nanowalls gives the larger accessible surface area to increase the current density, which produces a higher amount of MnO_2 depositions. The MnO_2 depositions merging with the adjacent nanowalls result in the increasing thickness of nanowalls in $MnO_2/VG_{1:1}$ due to the higher density of $VG_{1:1}$.

The TEM and HRTEM images illustrating the MnO_2-coated VG, cross-sectional view of nanowalls, and crystals of MnO_2 are shown in Fig. 2, which demonstrate the morphologies and microstructures of as-deposited MnO_2 and VG in more detail. The MnO_2-coated VG scratched from the substrates are dispersed in ethanol by ultrasonification treatment for preparing a TEM sample. The adhesive contacts of MnO_2 on VG indicate the strong bonding between MnO_2 and VG as shown in Fig. 2(a), which agrees with our previous investigations that the intimate adhesion is formed through the electrochemical deposition process.[33] Furthermore, Fig. 2(b) shows the HRTEM images exhibiting the well-stacked layers ranging from 10 to 20 with the interplanar spacing of approximately 0.36 nm, which corresponds to the lattice constant of graphene, indicating the formation of graphene nanowalls.[43] In addition, the layer distance of ~0.43 nm observed in Fig. 2(c) conforms to the lattice parameter of β-MnO_2, suggesting the formation of crystals of MnO_2 *via* electrochemical deposition.[44,45] According to the HRTEM images, the VG nanowalls fabricated with a thickness ranging from ~3 to ~8 nm *via* the PECVD process

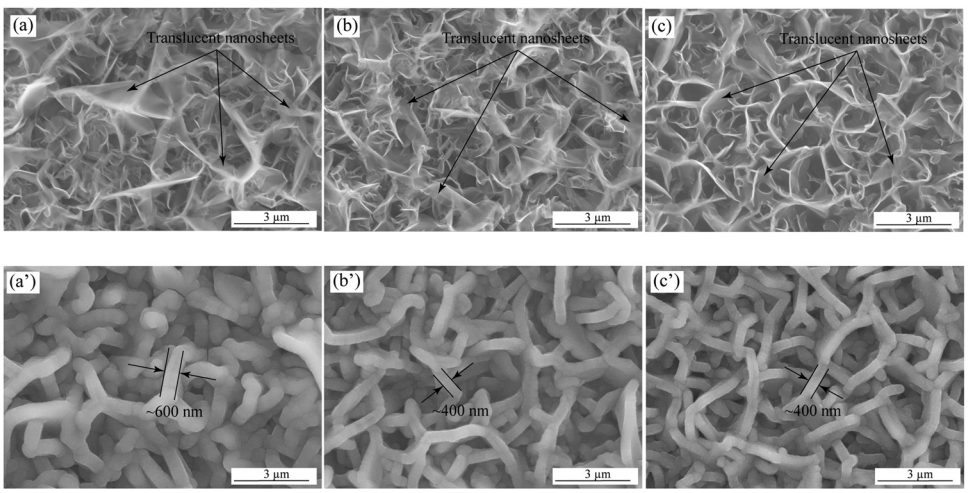

Fig. 1 SEM images of as-deposited VG nanowalls of (a) $VG_{1:1}$, (b) $VG_{1:2.5}$, and (c) $VG_{1:5}$; MnO_2-coated VG nanowalls of (a′) $MnO_2/VG_{1:1}$, (b′) $MnO_2/VG_{1:2.5}$, and (c′) $MnO_2/VG_{1:5}$.

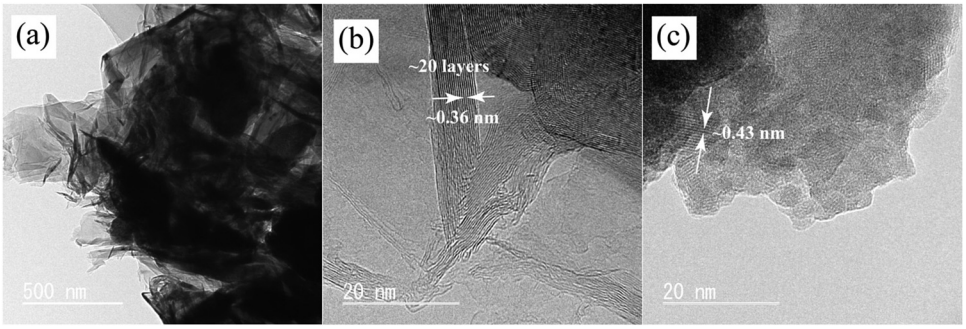

Fig. 2 TEM and HRTEM images of $MnO_2/VG_{1:2.5}$: (a) MnO_2-coated VG; (b) cross-section view of VG nanowalls; and (c) crystal structures of MnO_2.

are successfully achieved. Moreover, the interaction between MnO_2 and VG nanowalls with robust bonding can improve the supercapacitor performance.

3.2 XPS and Raman analysis

XPS analysis is further conducted to reveal the elemental compositions and valence states of $MnO_2/VG_{1:2.5}$. As shown in Fig. 3(a), the broad-ranged XPS spectra exhibit the main peaks of Mn 2s, Mn 2p, O 1s, and C 1s, indicating the formation of carbon-based scaffolds and manganese oxide. In Fig. 3(b), the C 1s spectrum can be deconvoluted into three peaks centered at 284.6 eV, 286.1 eV, and 288.0 eV, corresponding to the bonding types of C–C, C═O, and O–C═O, respectively.[46,47] The C–C bonding agrees with the SEM and TEM results, showing the successful growth of VG nanowalls.[48] Furthermore, the two peaks deconvoluted from the O 1s high-resolution spectrum with the binding energy at the centers of 529.7 eV and 530.9 eV present the Mn–O–Mn and C–O bonds as shown in Fig. 3(c).[49,50] Moreover, the spin energy separation of 11.7 eV in Mn 2p split into Mn $2p_{1/2}$ (654.6 eV) and Mn $2p_{3/2}$ (642.9 eV) suggests the presence of Mn^{4+}, indicating the formation of MnO_2 *via* electrochemical methods.[33,47]

Fig. 3(e) shows the Raman spectra of $VG_{1:2.5}$ and $MnO_2/VG_{1:2.5}$. The two distinct peaks, centered at 1347 cm^{-1} and 1577 cm^{-1} in $VG_{1:2.5}$, assigned to D and G bands of graphene, exhibit the intensity ratio I_D/I_G of as low as 0.29, indicating the low level of disorder and defect degree of graphene and the formation of superior graphene nanowalls.[31,51,52] The low-intensity ratio of I_D/I_G suggests the fabrication of graphene nanowalls with a smaller amount of sp^3-type defects in agreement with our TEM images, which may lead to stronger mechanical and better electrical properties.[20,52,53] Furthermore, the three peaks located at 502.1 cm^{-1}, 571.7 cm^{-1}, and 640.8 cm^{-1} in the range of 400 cm^{-1} and 800 cm^{-1} in $MnO_2/VG_{1:2.5}$ are attributed to the Mn–O stretching vibration, suggesting the successful formation of MnO_2.[20,54,55]

3.3 Electrochemical properties of the $MnO_2/VG_{1:1}$, $MnO_2/VG_{1:2.5}$, and $MnO_2/VG_{1:5}$ electrodes

The CV and GV curves are obtained to evaluate the electrochemical performance of $MnO_2/VG_{1:1}$, $MnO_2/VG_{1:2.5}$, and $MnO_2/VG_{1:5}$ electrodes in a typical 1 M Na_2SO_4 aqueous solution with a three-electrode system operated in the potential window of 0–1 V. As shown in Fig. 4(a)–(c), the rectangular-shaped CV curves at scan rates from 5 mV s^{-1} to 100 mV s^{-1} for all the three electrodes suggest the excellent pseudocapacitive performance and faradaic redox reaction during the charge–discharge process.[23,53] Meanwhile, the CV curves at the fast scan rate of 100 mV s^{-1} retain a quasi-rectangular configuration, indicating the good rate capacitance for all the three electrodes.[19] The superior electrochemical behaviors are associated with the nanostructures composed of the VG nanowalls and highly dispersed MnO_2 depositions as discussed in our previous study.[33] For comparison, the CV curves for the three electrodes at a scan rate of 5 mV s^{-1} are illustrated in Fig. 3(d). The three CV curves belonging to the electrodes present different current densities from the negative to positive current flows. It is well-known that the integrated loop area of CV curves represents the specific capacitance of supercapacitor electrodes in ideal capacitive behaviors. For the cases of non-ideality, the forward scan may have a higher area than the reverse scan. Therefore, the calculation for specific capacitance in non-ideality can be made with the data from the discharging scan.[56] In the lowest current density of CV curves for our three types of electrodes, the CV curves with the nearly symmetric shapes suggests that the areas of CV loops can represent the specific capacitance of supercapacitor electrodes. The lowest current density of the $MnO_2/VG_{1:5}$ exhibit the smallest integrated loop area, indicating an inferior specific capacitance.[5] On the other hand, the electrode of $MnO_2/VG_{1:2.5}$ with the VG growth in a medium level of density demonstrates the strongest current density in CV curves, suggesting the largest specific capacitance. The better electrochemical performance of $MnO_2/VG_{1:2.5}$ can be ascribed to the VG scaffold with the medium density, which provides plenty of surface area compared to $VG_{1:5}$. On the other hand, $MnO_2/VG_{1:2.5}$ holds sufficient distances between nanowalls, leaving enough space for the growth of MnO_2 instead of forming thicker MnO_2 depositions, compared to $MnO_2/VG_{1:1}$. As shown in Fig. 1(a) and (a′), the smaller gaps between nanowalls ($VG_{1:1}$) and thicker MnO_2 depositions ($MnO_2/VG_{1:1}$), which may increase the inner resistance due to the poor electrical conductivity of MnO_2 and hinder the access of electrolytes to active materials, affect the charge transport and redox reaction, resulting in the lower negative and positive

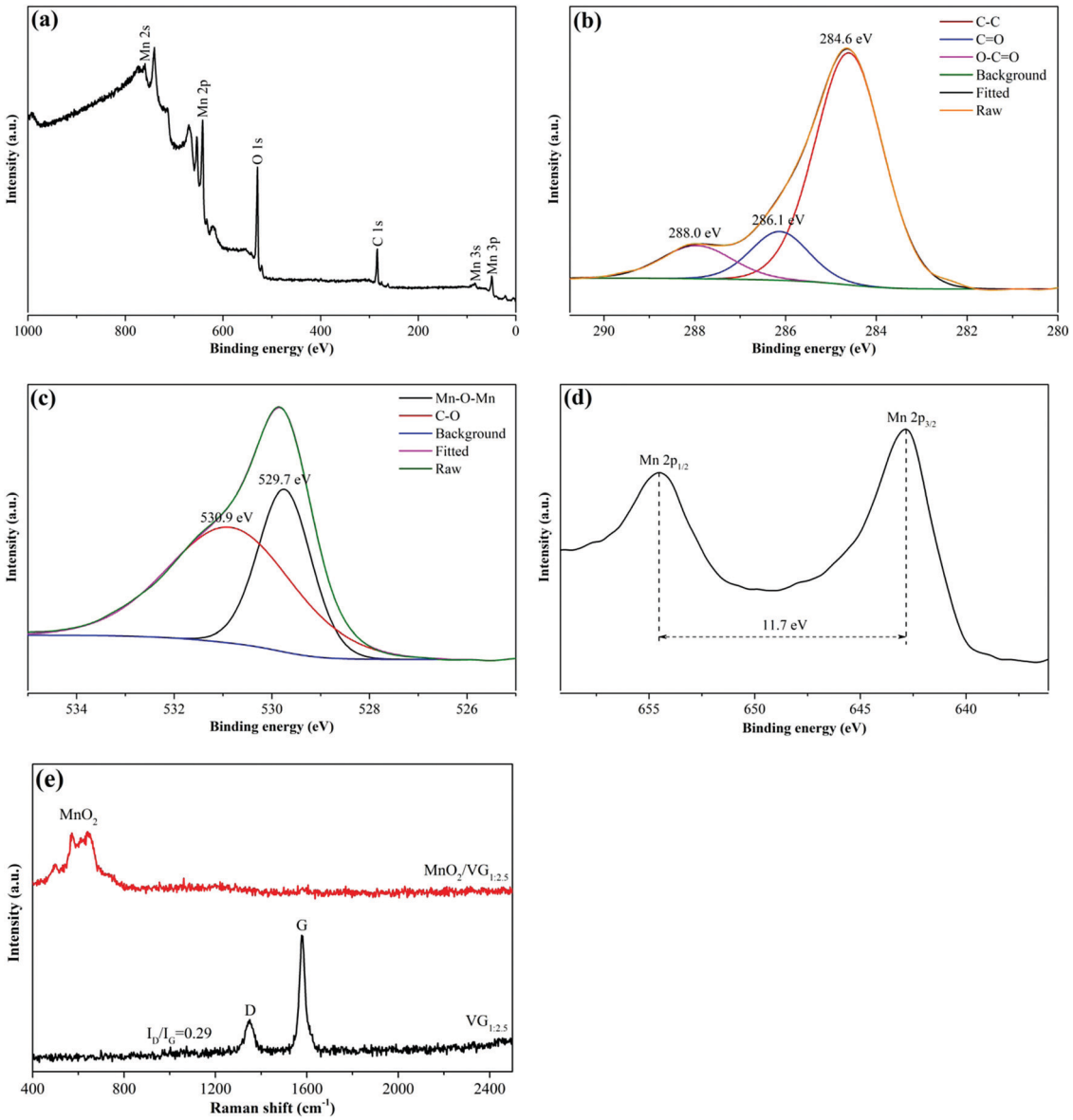

Fig. 3 XPS spectra for $MnO_2/VG_{1:2.5}$: (a) survey spectrum; (b) C 1s; (c) O 1s; and (d) Mn 2p. (e) Raman spectra of $MnO_2/VG_{1:2.5}$ and $VG_{1:2.5}$.

current density. In contrast, the weakest CV current density is owing to the VG and MnO_2-coated VG with a lowest level of density giving a smaller amount of active materials, as observed in Fig. 1(c) and (c′) for $VG_{1:5}$ and $MnO_2/VG_{1:5}$. These results suggest that the medium levels of graphene densities are able to offer a balance between the accessibility of electrolytes to active materials and the adequacy of pseudocapacitive materials, producing the supercapacitor electrodes with promoted electrochemical performance.

As shown in Fig. 5(a)–(c), further electrochemical evaluations with GV charge–discharge curves obtained at current densities sweeping from 0.5 mA cm^{-2} to 5 mA cm^{-2} for the three electrodes are conducted. The nearly symmetrical and quasi-triangular profiles for all the GV curves suggest superior reversibility and pseudocapacitive behaviors.[57,58] Among the three electrodes, the longest discharging time of $MnO_2/VG_{1:2.5}$ (Fig. 5(b)) suggests the better electrochemical performance, which complies with the CV curves showing the largest negative-to-positive current density. The area-normalized specific capacitance based on GV measurements can be calculated by using the formula shown below.[59,60]

$$C = \frac{I\Delta t}{A\Delta V},$$

where I and Δt are the discharging current density and duration. A and ΔV represent the operation area of an electrode and potential window. As shown in Fig. 4(d), the area-normalized specific capacitance of the three electrodes of $MnO_2/VG_{1:1}$, $MnO_2/VG_{1:2.5}$, and $MnO_2/VG_{1:5}$ can be calculated to be 148 mF cm^{-2}, 166 mF cm^{-2}, and 142 mF cm^{-2} at a current density of 0.5 mA cm^{-2}, respectively. The specific capacitance of $MnO_2/VG_{1:2.5}$ at higher current rates up to 5 mA cm^{-2} retains

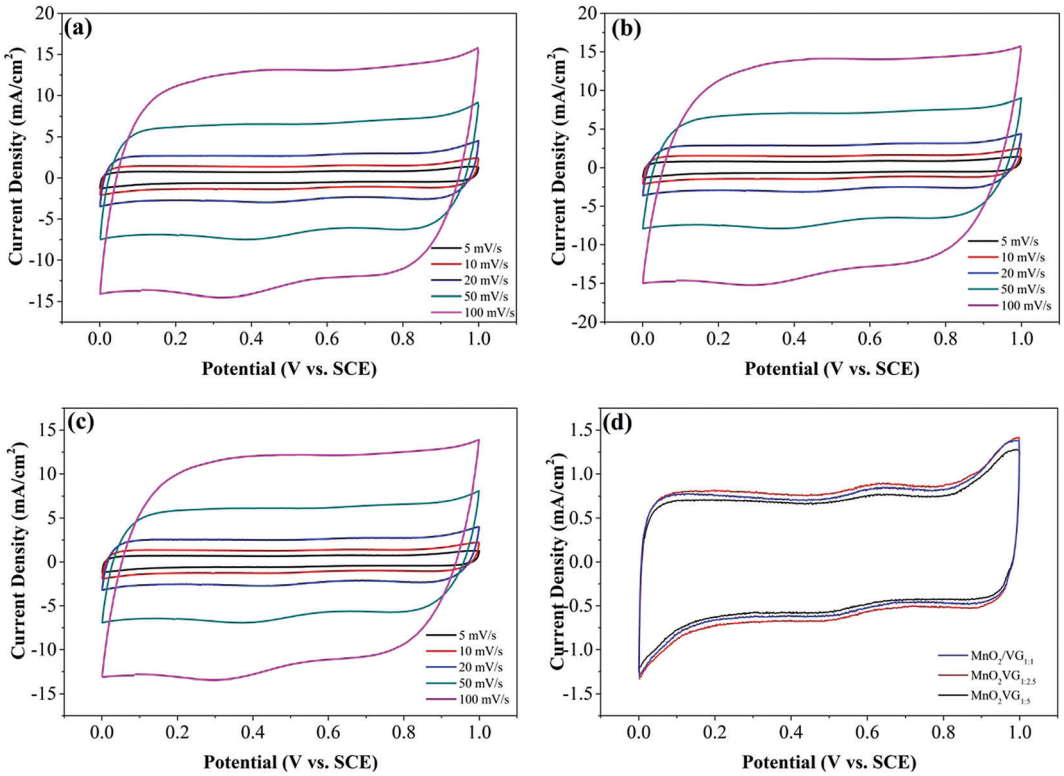

Fig. 4 CV curves of (a) $MnO_2/VG_{1:1}$, (b) $MnO_2/VG_{1:2.5}$, and (c) $MnO_2/VG_{1:5}$ at various scan rates from 5 mV s^{-1} to 100 mV s^{-1}; (d) comparison of the three electrodes at a scan rate of 5 mV s^{-1}.

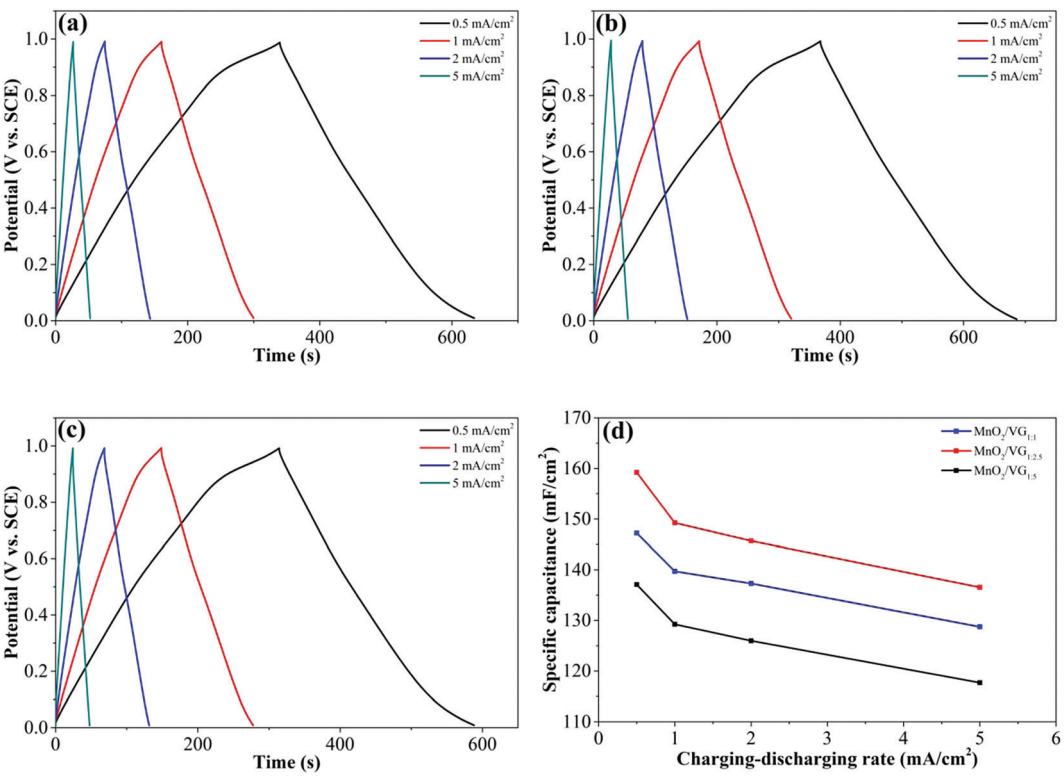

Fig. 5 GV curves of (a) $MnO_2/VG_{1:1}$, (b) $MnO_2/VG_{1:2.5}$, (c) $MnO_2/VG_{1:5}$, and (d) area-normalized specific capacitance of three electrodes at different charge–discharge rates from 0.5 mA cm^{-2} to 5 mA cm^{-2}.

the highest values compared to the other two electrodes, indicating the improved charge–discharge properties under all the working conditions. The reduction of the area-normalized specific capacitance of $MnO_2/VG_{1:2.5}$ from 166 mF cm^{-2} to 142 mF cm^{-2} occurs due to the increase of the charge–discharge rate from 0.5 mA cm^{-2} to 5 mA cm^{-2}, which demonstrates an excellent capacitance retention of 86.04%. Besides, the other two electrodes of $MnO_2/VG_{1:1}$ and $MnO_2/VG_{1:5}$ exhibit similar retentions of 87.4% and 85.84% respectively, indicating the superior rate capability with the increasing charge–discharge rates.

The ratios of gaseous precursors, densities of VG nanowalls, and area-normalized specific capacitance are summarized in Table 1. It has to be mentioned that the growing time, chamber pressure, and operation power of plasma, *etc.*, which are also the factors determining the growing densities of VG nanowalls, are set as constants for all the three electrodes. The quantitative values of VG layers agree with the observations in Fig. 1(a)–(c) that the increasing distances of gaps are observed from $VG_{1:1}$ to $VG_{1:5}$. With increasing ratios of H_2, the VG densities on substrates are reduced due to the etching function of H-atoms, as discussed in the previous reports.[37,38] The lowest densities of $VG_{1:5}$ and $MnO_2/VG_{1:5}$ exhibit the poorest specific capacitance because of the less available nanowalls for growing active materials. Compared with $MnO_2/VG_{1:5}$, the increase of specific capacitance (~17%), with the larger density of $VG_{1:2.5}$ followed by the MnO_2 deposition, is observed due to the increasing amount of nanowalls and active materials in $MnO_2/VG_{1:2.5}$. However, the inversion of specific capacitance turning to a decrease in $MnO_2/VG_{1:1}$ with the largest density of VG nanowalls occurs, when the optimal VG density with a medium level in $MnO_2/VG_{1:2.5}$ is reached. The higher density of $MnO_2/VG_{1:1}$ leads to the worse access of electrolytes to the active materials, resulting in the poor redox reaction and lower specific capacitance (~10%). Consequently, $MnO_2/VG_{1:2.5}$ shows the highest area-normalized specific capacitance of 166 mF cm^{-2}, compared to the other two electrodes.

Electrochemical impedance spectroscopy (EIS) measurements representing the electrochemical properties between electrodes and electrolytes in the charge–discharge procedure are conducted for the three electrodes. The Nyquist plots of $MnO_2/VG_{1:1}$, $MnO_2/VG_{1:2.5}$, and $MnO_2/VG_{1:5}$ are displayed in Fig. 6. The intersections between the curves and *x*-axis are ascribed to equivalent series resistance (R_s) including the resistance of electrodes, electrolytes, and the contact resistances of electrodes and substrates.[61] All the three electrodes show the small R_s with ~3.2 Ω ($MnO_2/VG_{1:1}$), ~3.0 Ω ($MnO_2/VG_{1:2.5}$), and ~4.0 Ω ($MnO_2/VG_{1:5}$), suggesting that the low

Table 1 Summarization of ratios, densities and area-normalized specific capacitance at 0.5 mA cm^{-2}

Ratio of $CH_4:H_4$	VG density (mg cm^{-2})	Specific capacitance (mF cm^{-2})
1 : 1	3.63	148
1 : 2.5	2.35	166
1 : 5	0.83	142

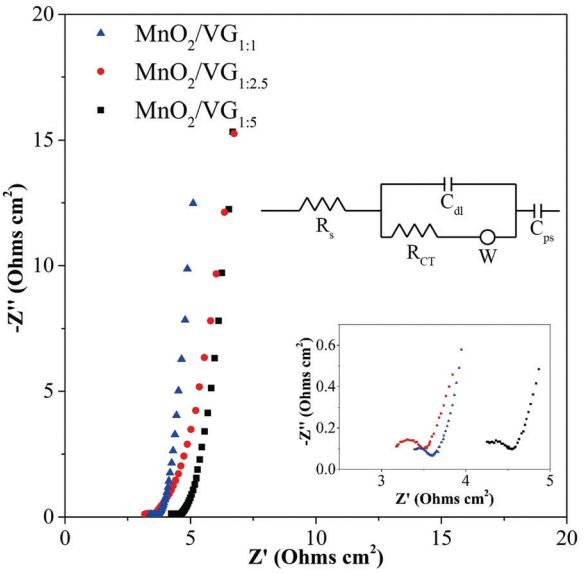

Fig. 6 Nyquist plots of $MnO_2/VG_{1:1}$, $MnO_2/VG_{1:2.5}$, and $MnO_2/VG_{1:5}$. Insets: Equivalent circuit.

resistance contributes to the direct growth and VG scaffolds on silicon wafer substrates and intimate contacts between VG and active materials as discussed in our previous work.[33] The lowest R_s of $MnO_2/VG_{1:2.5}$ can be interpreted by the medium density of nanowalls and the appropriate thickness of active materials. In contrast, the higher thickness of MnO_2 depositions and smaller distances between VG nanowalls result in a larger R_s, due to the weak electrical conductivity of MnO_2 in $MnO_2/VG_{1:1}$. The lowest density of VG scaffolds ($MnO_2/VG_{1:5}$) gives the fewer nanowalls serving as electrical conductors, leading to the higher equivalent series resistance. Furthermore, the diameters of semicircle arcs named R_{CT} correspond to the resistance of electrolytes diffusing into the pores of electrodes and the charge transfer resistance.[62–65] The similar R_{CT} values at around 0.5 Ω for the three electrodes indicate that the fast interactions between electrodes and electrolytes, contributed to the highly distributed active materials and porous structure of MnO_2 depositions. In the low-frequency region, the nearly perpendicular lines for all the three electrodes suggest the ideal capacitive behavior (either EDLC or pseudocapacitive) and low Warburg resistance (W), indicating the excellent ion diffusivity and capacitive behaviors.[19,57] The slightly inclined curve of $MnO_2/VG_{1:2.5}$, compared to that of the other two electrodes, reveals the more pseudocapacitive behaviors leading to the highest area-normalized specific capacitance, because of the increasing amount of active materials involved in the faradaic redox reaction.

The cycling stability of the $MnO_2/VG_{1:2.5}$ electrode tested in a three-electrode system is evaluated at a constant charge–discharge rate of 5 mA cm^{-2} with the working window of 0–1 V for consecutive 5000 cycles to confirm the long-term charge–discharge performance. As shown in Fig. 7, the high retention (98.68%) of the original capacitance at the end of 5000 cycles suggests the superior durability ascribed the direct

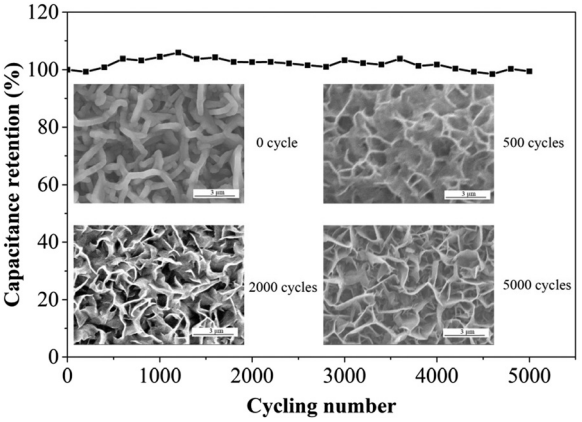

Fig. 7 Durability test for $MnO_2/VG_{1:2.5}$ electrode at a constant charge–discharge rate of 5 mA cm^{-2} for consecutive 5000 cycles. Insets: Surface morphologies of $MnO_2/VG_{1:2.5}$ at the initial status and after 500, 2000, and 5000 cycles.

growth of VG on silicon substrates and strong bonding between active materials and scaffolds. The surface morphologies of $MnO_2/VG_{1:2.5}$ after 500, 2000, and 5000 cycles, showing the changes in microstructures under long-term cycles, are demonstrated in the insets. The redistribution of active materials from the initial status to 500 cycles can be observed, which results in the changes in the microstructures. However, the reversible charge–discharge process of MnO_2 leads to the constant specific capacitance at the initial cycling stage. The ignorable morphology changes in the SEM images for 500, 2000, and 5000 cycles suggest the stable and robust adhesion of MnO_2, achieve the long-term stability of the supercapacitor electrode.

3.4. Assembly of asymmetric supercapacitors with MnO_2/VG/Si and carbon black electrodes

The feasibility study of the supercapacitor electrodes containing the directly grown VG and electrochemically deposited MnO_2 in a supercapacitor device is of importance investigating the practical potentials of the prepared supercapacitor electrodes. The asymmetric supercapacitor devices with MnO_2/VG/Si as the positive electrode and carbon black as the negative electrode are assembled in a coin cell including 1 M Na_2SO_4 aqueous solution as the electrolyte and a piece of filter paper as the separator. The shortened deposition time of MnO_2 (400 s) in the above-mentioned electrodes benefits the microstructural observations, due to the longer duration of electrochemical depositions resulting in the complete filling of the gaps.[33] In contrast, the increasing amounts of active materials deposited on electrodes provide a higher specific capacitance, which can be used to assemble supercapacitor devices with a better energy storage capability. Meanwhile, the robust adhesions of VG on silicon wafer substrates can afford heavy amounts of MnO_2 depositions to obtain supercapacitor electrodes with an excellent electrochemical performance.[33] To demonstrate the stability of VG scaffolds and the good electrochemical properties, the positive electrode with $VG_{1:2.5}$ as the scaffold and MnO_2 electro-deposited under a constant potential of 0.6 V for 4000 s is prepared for the assembly of the asymmetric supercapacitor. The porous structures of MnO_2 depositions with longer growing times, which may fill the gaps between nanowalls as observed in our previous study, are still able to provide free access of ions in the electrolyte to interact with electrodes.[33] The deposition amount of MnO_2 for 4000 s with the operation potential of 0.6 V is calculated as 3.93 mg. The mass balance of carbon black nanoparticles loaded in the negative electrode is about 34.1 mg. Due to the energy storage nature of EDLC in negative electrodes, the loading amounts of carbon black are greatly larger than those of MnO_2 in positive electrodes, in order to give the corresponding energy storage capability. Fig. 8(a) shows the electrochemical performance of positive and negative electrodes conducting charge–discharge process in the Na_2SO_4 electrolyte with three electrode system before assembling in coin cells. The positive electrodes with the working potential ranging from $\sim$0 to $\sim$1.3 V and negative electrodes with the potential windows of $\sim$0 and ~ -0.7 V with all the current densities between 0.5 and 5 mA cm^{-2}, have the expected potential ranges to store electrical power. The CV curves performed with the scan rates of 5, 10, 20, 50, and 100 mV s^{-1} under the voltage window of 0–1.8 V for the device are shown in Fig. 8(b). The absence of the polarization phenomenon at all the CV curves indicates that the device can reach the working voltage up to 1.8 V.[66] The GV charge–discharge plots with the symmetrical and linear profiles for all the current densities varying from 0.5 to 5 mA cm^{-2} suggest the good electrochemical performance of the as-prepared supercapacitor device as shown in Fig. 8(c). The small IR drops for all the curves at the inverting points from the charge–discharge procedure imply the small R_s, which are ascribed to the optimum preparation process of the device.[5] More importantly, the direct growth of VG on silicon wafers forms the tight and intimate connections between active materials and current collectors, which greatly reduce the R_s. Furthermore, the specific capacitance of the supercapacitor device can be calculated with the equation as mentioned above. The area-normalized specific capacitances with the values of 230.93 mF cm^{-2} (0.5 mA cm^{-2}) and 164.92 mF cm^{-2} (5 mA cm^{-2}) are obtained, presenting the excellent capacitance retention of 71.42% with the increasing current density from 0.5 mA cm^{-2} to 5 mA cm^{-2}. Furthermore, the energy and power density are calculated by following the formulas[67]

$$E = \frac{C_A \times (\Delta V)^2}{2}$$

$$P = \frac{E}{\Delta t}$$

where E, P, and C_A are energy density, power density, and specific capacitance, respectively. ΔV and Δt represent potential window and discharge time. The maximum energy density and power density are calculated as E = 103.92 μW h cm^{-2} (P = 0.45 mW cm^{-2} and 0.5 mA cm^{-2}) and P = 4.5 mW cm^{-2} (E = 74.22 μW h cm^{-2} and 5 mA cm^{-2}). The asymmetric

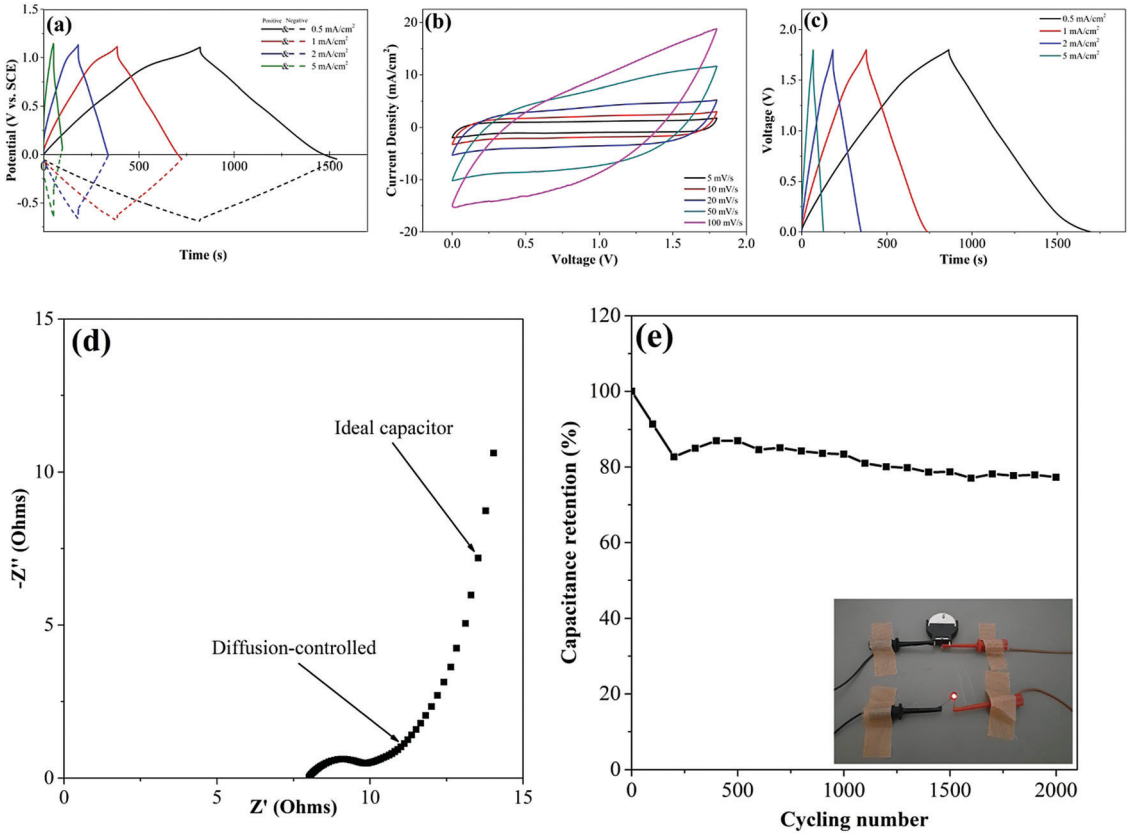

Fig. 8 (a) GV curves of positive and negative electrodes in the Na_2SO_4 electrolyte before assembling in coin cells; (b) CV curves; (c) GV curves; (d) Nyquist plot; and (e) cycling stability with inset of powering a red LED of the asymmetric supercapacitor device.

Table 2 Comparing asymmetric supercapacitor device with the previous reported literature

Material	Energy density (μW h cm^{-2})	Power density (mW cm^{-2})	Specific capacitance (mF cm^{-2})	Capacitance retention (%) [cycles]	Ref.
MnO_2/VGNs/Ni	7.7	5	56	80 [2000]	5
GNW/RuO_x	15.1	2.49	109	N/A	31
CF/MnO_2	2.7	8.3	4.9	89 [3000]	69
MnO_2/VG/Si	103.9	4.5	230.9	77.3 [2000]	This work

supercapacitor device exhibits a superior electrochemical performance, compared to the reported studies as listed in Table 2.

The properties of the supercapacitor device measured using electrochemical impedance spectroscopy (EIS) using the Nyquist plot are evaluated as shown in Fig. 8(d). The low R_s of $\sim 8\ \Omega$ indicates the good equivalent series resistance, which is attributed to the intimate contacts between the VG scaffold and active materials. The R_{CT} ($\sim 2\ \Omega$) illustrating that the ion transfer resistance suggests the superior interactions between electrodes and electrolytes. Furthermore, the slope angle with 45 °C at the middle-frequency region, which shows the diffusion-controlled process, is ascribed by the longer deposition time producing thicker MnO_2 layer and the porous structures of MnO_2.[33,68] The nearly vertical line at the low-frequency area, representing the ideal capacitive behavior, shows excellent pseudocapacitive performance. The durability test of the supercapacitor device is conducted to show the relatively high capacitance retention of 77.32% over 2000 cycles. The asymmetric supercapacitor is able to power a red LED as demonstrated in the inset of Fig. 8(e).

4. Conclusions

In summary, tunable densities of vertical graphene nanowalls deposited on silicon wafer substrates *via* PECVD have been achieved, which breaks the limits that the traditional fabrication methods have difficulties controlling the gap distances between graphene nanowalls. The improvement of MnO_2 electrochemical deposition, distributed on the surface of nanowalls uniformly by using a mixture of ethanol and distilled water as the solvent, provides access to reveal the density effects of scaffolds on the electrochemical performance of supercapacitor electrodes. The vertical graphene scaffolds with different

densities are controlled by varying the flow ratios of precursor gaseous materials to be 1:1, 1:2.5, and 1:5 for $CH_4:H_2$, followed by the electrochemical deposition of MnO_2 under a constant condition. We have found that the electrode of MnO_2/$VG_{1:2.5}$ with the medium density of VG scaffold shows the maximum area-normalized specific capacitance of 166 mF cm^{-2} among the three electrodes. The electrode of MnO_2/$VG_{1:2.5}$ exhibits excellent rate capacitance with the retention of 86% when the charge–discharge rate increases from 0.5 mA cm^{-2} to 5 mA cm^{-2}. To investigate the applicable potentials, the asymmetric supercapacitor device with MnO_2/VG/Si as the positive electrode and carbon black as the negative electrode has been assembled. The supercapacitor device demonstrates an excellent area-normalized specific capacitance of 230.9 mF cm^{-2} with a maximum energy density of 103.9 μW h cm^{-2} and power density of 4.5 mW cm^{-2}. The relatively high cycling stability with the capacitance retention of 77.3% under consecutive 2000 cycles is achieved. This approach represents the fundamental understanding of the density effects of scaffolds on the pseudocapacitive supercapacitor electrodes. Meanwhile, the superior electrochemical performance of the asymmetric supercapacitor device demonstrates the promising potentials to fabricate energy-storage electronics by using the electrodes based on vertical graphene and pseudocapacitive materials.

Conflicts of interest

There are no conflicts to declare.

Acknowledgements

This work was mainly performed in the Micro/Nanomachining Research Education Center (MNC) of Tohoku University and Micro System Integration Center, Tohoku University. This work is supported by Cross-ministerial Strategic Innovation Promotion Program (SIP), Japan (The New Energy and Industrial Technology Development Organization, NEDO).

References

1 P. B. Koeneman, I. J. Busch-Vishniac and K. L. Wood, Feasibility of Micro Power Supplies for MEMS, *J. Microelectromech. Syst.*, 1997, **6**(4), 355–362.
2 X. Wang and G. Shi, Flexible graphene devices related to energy conversion and storage, *Energy Environ. Sci.*, 2015, **8**, 790–823.
3 H. E. Brouji, O. Briat, J.-M. Vinassa, H. Henry and E. Woirgard, Analysis of the dynamic behavior changes of supercapacitors during calendar life test under several voltages and temperatures conditions, *Microelectron. Reliab.*, 2009, **49**(9–11), 1391–1397.
4 Y. Liu, X. Cai, B. Luo, M. Yan, J. Jiang and W. Shi, MnO_2 decorated on carbon sphere intercalated graphene film for high-performance supercapacitor electrodes, *Carbon*, 2016, **107**, 426–432.
5 Y. Zhou, X. Cheng, F. Huang, Z. Sha, Z. Han, J. Chen, W. Yang, Y. Yu, J. Zhang, S. Peng, S. Wu, A. Rider, L. Dai and C. H. Wang, Hierarchically structured electrodes for moldable supercapacitors by synergistically hybridizing vertical graphene nanosheets and MnO_2, *Carbon*, 2021, **172**, 272–282.
6 Z. Wu, K. Parvez, S. Li, S. Yang, Z. Liu, S. Liu, X. Feng and K. Mullen, Alternating Stacked Graphene-Conducting Polymer Compact Films with Ultrahigh Areal and Volumetric Capacitances for High-Energy Micro-Supercapacitors, *Adv. Mater.*, 2015, **27**, 4054–4061.
7 Y. Jiang and J. Liu, Definitions of Pseudocapacitive Materials: A Brief Review, *Energy Environ.*, 2019, **2**(1), 30–37.
8 Z. Fahimi and O. Moradlou, Fabrication of ZnO@C foam: a flexible free-standing electrode for energy storage devices, *Mater. Des.*, 2020, **189**, 108525.
9 M. Kim, Y. Hwang and J. Kim, Process dependent graphene/MnO_2 composites for supercapacitors, *Chem. Eng. J.*, 2013, **230**, 482–490.
10 W. Guo, C. Yu, S. Li, Z. Wang, J. Yu, H. Huang and J. Qiu, Strategies and insights towards the intrinsic capacitive properties of MnO_2 for supercapacitors: Challenges and perspectives, *Nano Energy*, 2019, **57**, 459–472.
11 D. Yan, Z. Guo, G. Zhu, H. Yang, R. Wei, H. Xu and A. Yu, Electrochemical properties of 3D MnO_2 film prepared by chemical bath deposition at room temperature, *Mater. Lett.*, 2012, **82**, 156–158.
12 G. Yu, L. Hu, N. Liu, H. Wang, M. Vosgueritchian, Y. Yang, Y. Cui and Z. Bao, Enhancing the supercapacitor performance of graphene/MnO_2 nanostructured electrodes by conductive wrapping, *Nano Lett.*, 2011, **11**, 4438–4442.
13 X. Zhou, T. Meng, F. Yi, D. Shu, Z. Li, Q. Zeng, A. Gao and Z. Zhu, Supramolecular assisted fabrication of Mn_3O_4 anchored nitrogen-doped reduced graphene oxide and its distinctive electrochemical activation process during supercapacitive study, *Electrochim. Acta*, 2021, **370**, 137739.
14 N. Jabeen, Q. Xia, S. V. Savilov, S. M. Aldoshin, Y. Yu and H. Xia, Enhanced Pseudocapacitive Performance of *a*-MnO_2 by Cation Preinsertion, *ACS Appl. Mater. Interfaces*, 2016, **8**(49), 33732–33740.
15 X. Zhu, Q. Xia, X. Liu, Q. Zhang, J. Xu, B. Lin, S. Li, Y. Zhuang, C. Qiu, L. Xue, L. Gu and H. Xia, Retarded layered-to-spinel phase transition in structure reinforced birnessite with high Li content, *Sci. Bull.*, 2021, **66**(3), 219–224.
16 N. J.-A. Hussain, Q. Xia, S. Sun, J. Zhu and H. Xia, High-Performance 2.6 V Aqueous Asymmetric Supercapacitors based on In Situ Formed $Na_{0.5}MnO_2$ Nanosheet Assembled Nanowall Arrays, *Adv. Mater.*, 2017, **29**(32), 1700804.
17 W. Wei, X. Cui, W. Chen and D. G. Ivey, Manganese oxide-based materials as electrochemical supercapacitor electrodes, *Chem. Soc. Rev.*, 2011, **40**, 1697–1721.
18 Z. Li, Y. Mi, X. Liu, S. Liu, S. Yang and J. Wang, Flexible graphene/MnO_2 composite papers for supercapacitor electrodes, *J. Mater. Chem.*, 2011, **21**, 14706–14711.

19 Z. Ye, T. Li, G. Ma, X. Peng and J. Zhao, Morphology controlled MnO_2 electrodeposited on carbon fiber paper for high-performance supercapacitors, *J. Power Sources*, 2017, **351**, 51–57.
20 Z. Zhao, T. Shen, Z. Liu, Q. Zhong and Y. Qin, Facile fabrication of binder-free reduced graphene oxide/MnO_2/Ni foam hybrid electrode for high-performance supercapacitors, *J. Alloys Compd.*, 2020, **812**, 15124.
21 Q. Zhang, X. Wu, Q. Zhang, F. Yang, H. Dong, J. Sui and L. Dong, One-step hydrothermal synthesis of MnO_2/graphene composite for electrochemical energy storage, *J. Electroanal. Chem.*, 2019, **837**, 108–115.
22 S. Chen, J. Zhu, X. Wu, Q. Han and X. Wang, Graphene Oxide-MnO_2 Nanocomposites for Supercapacitors, *ACS Nano*, 2010, **4**(5), 2822–2830.
23 O. Sadak, W. Wang, J. Guan, A. K. Sundramoorthy and S. Gunasekaran, MnO_2 Nanoflowers Deposited on Graphene Paper as Electrode Materials for Supercapacitors, *ACS Appl. Nano Mater.*, 2019, **2**, 4386–4394.
24 A. Oz, D. Gelman, E. Goren, N. Shomrat, S. Baltianski and Y. Tsur, A novel approach for supercapacitors degradation characterization, *J. Power Sources*, 2017, **355**, 74–82.
25 Q. Zhang, J. Sun, Z. Pan, J. Zhang, J. Zhao, X. Wang, C. Zhang, Y. Yao, W. Lu, Q. Li, Y. Zhang and Z. Zhang, Stretchable fiber-shaped asymmetric supercapacitors with ultrahigh energy density, *Nano Energy*, 2017, **39**, 219–228.
26 T. Liu and Y. Li, Addressing the Achilles' heel of pseudocapacitive materials: Long-term stability, *InfoMat*, 2020, **2**(5), 807–842.
27 H. Shen, H. Li, M. Li, C. Li, L. Qian, L. Su and B. Yang, High-performance aqueous symmetric supercapacitor based on polyaniline/vertical graphene/Ti multilayer electrodes, *Electrochim. Acta*, 2018, **283**, 410–418.
28 Z. J. Han, S. Pineda, A. T. Murdock, D. H. Seo, K. Ostrikov and A. Bendavid, RuO_2-coated vertical graphene hybrid electrodes for high-performance solid-state supercapacitors, *J. Mater. Chem. A*, 2017, **5**(33), 17293–17301.
29 Z. Bo, Z. Wen, H. Kim, G. Lu, K. Yu and J. Chen, One-step fabrication and capacitive behavior of electrochemical double layer capacitor electrodes using vertically-oriented graphene directly grown on metal, *Carbon*, 2012, **50**(12), 4379–4387.
30 J. Li, N. V. Toan, Z. Wang and T. Ono, Metal-assisted-chemical-etching of silicon nanowires for templating 3D graphene growth towards energy storage in microsystems, *J. Micromech. Microeng.*, 2019, **29**, 055007.
31 J. Li, M. Zhu, Z. An, Z. Wang, M. Toda and T. Ono, Constructing in-chip micro-supercapacitors of 3D graphene nanowall/ruthenium oxides electrode through silicon-based microfabrication technique, *J. Power Sources*, 2018, **401**, 204–212.
32 J. Li, M. Zhu, Z. Wang and T. Ono, Engineering micro-supercapacitors of graphene nanowalls/Ni heterostructure based on microfabrication technology, *Appl. Phys. Lett.*, 2016, **109**, 153901.
33 H. Sui, N. V. Toan and T. Ono, Vertically-oriented graphene electrodeposited with MnO_2 on native SiO_2/Si for high-performance supercapacitor electrodes, *J. Electroanal. Chem.*, 2021, **895**, 115507.
34 Y. Zhang, Q. Zou, H. S. Hsu, S. Raina, Y. Xu, J. B. Kang, J. Chen, S. Deng, N. Xu and W. P. Kang, Morphology Effect of Vertical Graphene on the High Performance of Supercapacitor Electrode, *ACS Appl. Mater. Interfaces*, 2016, **8**, 7363–7369.
35 D. Majumdar, T. Maiyalagan and Z. Jiang, Recent Progress in Ruthenium Oxide-Based Composites for Supercapacitor Applications, *ChemElectroChem*, 2019, **6**(17), 4343–4372.
36 X. Hu, L. Wei, R. Chen, Q. Wu and J. Li, Reviews and Prospectives of Co_3O_4-Based Nanomaterials for Supercapacitor Application, *ChemistrySelect*, 2020, **5**(17), 5268–5288.
37 J. Wang, M. Zhu, R. A. Outlaw, X. Zhao, D. M. Manos and B. C. Holloway, Synthesis of carbon nanosheets by inductively coupled radio-frequency plasma enhanced chemical vapor deposition, *Carbon*, 2004, **42**(14), 2867–2872.
38 Y. Wu, B. Yang, B. Zong, H. Sum, Z. Shen and Y. Feng, Carbon nanowalls and related materials, *J. Mater. Chem.*, 2004, **14**, 469–477.
39 Z. Bo, K. Yu, G. Lu, P. Wang, S. Mao and J. Chen, Understanding growth of carbon nanowalls at atmospheric pressure using normal glow discharge plasma-enhanced chemical vapor deposition, *Carbon*, 2011, **49**(6), 1849–1858.
40 V. Krivchenko, P. Shevnin, A. Pilevsky, A. Egorov, N. Suetin, V. Sen, S. Evlashin and A. Rakhimov, Influence of the growth temperature on structural and electron field emission properties of carbon nanowall/nanotube films synthesized by catalyst-free PECVD, *J. Mater. Chem.*, 2012, **22**, 16458–16464.
41 Z. Bo, Y. Yang, J. Chen, K. Yu, J. Yan and K. Cen, Plasma-enhanced chemical vapor deposition synthesis of vertically oriented graphene nanosheets, *Nanoscale*, 2013, **5**, 5180–5204.
42 Y. Zhang, J. Du, S. Tang, P. Liu, S. Deng, J. Chen and N. Xu, Optimize the field emission character of a vertical few-layer graphene sheet by manipulating the morphology, *Nanotechnology*, 2012, **23**, 015202.
43 L. Wang, B. Wei, P. Dong, Q. Miao, Z. Liu, F. Xu, J. Wu, J. Lou, R. Vajtai and W. Fei, Large-scale synthesis of few-layer graphene from magnesium and different carbon sources and its application in dye-sensitized solar cells, *Mater. Des.*, 2016, **92**, 462–470.
44 Q. Zhang, S. Li, S. Sun, X. Yin and J. Yu, Lithium selective adsorption on 1-D MnO_2 nanostructure ion-sieve, *Adv. Powder Technol.*, 2009, **20**(5), 432–437.
45 B. R. Chen, W. Sun, D. A. Kitchaev, J. S. Mangum, V. Thampy, L. M. Garten, D. S. Ginley, B. P. Gorman, K. H. Stone, G. Ceder, M. F. Toney and L. T. Schelhas, Understanding crystallization pathways leading to manganese oxide polymorph formation, *Nat. Commun.*, 2018, **9**, 2553.
46 Z. Niu, T. Yue, W. Hu, W. Sun, Y. Hu and Z. Xu, Covalent bonding of MnO_2 onto graphene aerogel forwards: Efficiently catalytic degradation of organic wastewater, *Appl. Surf. Sci.*, 2019, **496**, 143585.
47 S. Qiu, R. Li, Z. Huang, Z. Huang, C. P. Tsui, C. He, X. Han and Y. Yang, Scalable sonochemical synthesis of petal-like

MnO_2/graphene hierarchical composites for high-performance supercapacitors, *Composites, Part B*, 2019, **161**, 37–43.

48 C. Yang, H. Bi, D. Wan, F. Huang, X. Xie and M. Jiang, Direct PECVD growth of vertically erected graphene walls on dielectric substrates as excellent multifunctional electrodes, *J. Mater. Chem. A*, 2013, **1**, 770–775.

49 S. Y. Huang, P. A. Le, P. J. Yen, Y. C. Lu, S. K. Sahoo, H. W. Cheng, P. W. Chiu, T. Y. Tseng and K. H. Wei, Cathodic plasma–induced syntheses of graphene nanosheet/MnO_2/WO_3 architectures and their use in supercapacitors, *Electrochim. Acta*, 2020, **342**, 136043.

50 L. Lu, H. Tian, J. He and Q. Yang, Graphene-MnO_2 Hybrid Nanostructure as a New Catalyst for Formaldehyde Oxidation, *J. Phys. Chem. C*, 2016, **120**, 23660–23668.

51 S. Ghosh, B. Gupta, K. Ganesan, A. Das, M. Kamruddin, S. Dash and A. K. Tyagi, MnO_2-Vertical graphene nanosheets composite electrodes for energy storage devices, *Mater. Today: Proc.*, 2016, **3**(6), 1686–1692.

52 A. Zandiatashbar, G. H. Lee, S. J. An, S. Lee, N. Mathew, M. Terrones, T. Hayashi, C. R. Picu, J. Hone and N. Koratkar, Effect of defects on the intrinsic strength and stiffness of graphene, *Nat. Commun.*, 2014, **5**, 3186.

53 S. Jadhav, R. S. Kalubarme, C. Terashima, B. B. Kale, V. Godbole, A. Fujishima and S. W. Gosavi, Manganese dioxide/reduced graphene oxide composite an electrode material for high-performance solid state supercapacitor, *Electrochim. Acta*, 2019, **299**, 34–44.

54 C. Julien, M. Massot, R. Baddour-Hadjean, S. Franger, S. Bach and J. P. Pereira-Ramos, Raman spectra of birnessite manganese dioxides, *Solid State Ion.*, 2003, **159**(3–4), 345–356.

55 B. Ouyang, Y. Zhang, Z. Zhang, H. J. Fan and R. S. Rawat, Green synthesis of vertical graphene nanosheets and their application in high-performance supercapacitors, *RSC Adv.*, 2016, **6**, 23968–23973.

56 A. Noori, M. F. El-Kady, M. S. Rahmanifar, R. B. Kaner and M. F. Mousavi, Towards establishing standard performance metrics for batteries, supercapacitors and beyond, *Chem. Soc. Rev.*, 2019, **48**(5), 1272–1341.

57 X. Su, L. Yu, G. Cheng, H. Zhang, M. Sun and X. Zhang, High-performance α-MnO_2 nanowire electrode for supercapacitors, *Appl. Energy*, 2015, **153**, 94–100.

58 Q. Cheng, J. Tang, J. Ma, H. Zhang, N. Shinya and L. Qin, Graphene and nanostructured MnO_2 composite electrodes for supercapacitors, *Carbon*, 2011, **49**(9), 2917–2925.

59 S. Zhao, T. Liu, D. Hou, W. Zeng, B. Miao, S. Hussain, X. Peng and M. S. Javed, Controlled synthesis of hierarchical birnessite-type MnO_2 nanoflowers for supercapacitor applications, *Appl. Surf. Sci.*, 2015, **356**, 259–265.

60 X. Wang, Y. Yin, C. Hao and Z. You, A high-performance three-dimensional micro supercapacitor based on ripple-like ruthenium oxide–carbon nanotube composite films, *Carbon*, 2015, **82**, 436–445.

61 B. A. Mei, O. Munteshari, J. Lau, B. Dunn and L. Pilon, Physical Interpretations of Nyquist Plots for EDLC Electrodes and Devices, *J. Phys. Chem. C*, 2018, **122**, 194–206.

62 I. Yang, S. G. Kim, S. H. Kwon, M. S. Kim and J. C. Jung, Relationships between pore size and charge transfer resistance of carbon aerogels for organic electric double-layer capacitor electrodes, *Electrochim. Acta*, 2017, **223**, 21–30.

63 B. Fang and L. Binder, A modified activated carbon aerogel for high-energy storage in electric double layer capacitors, *J. Power Sources*, 2006, **163**(1), 616–622.

64 C. Liu, W. Dong, G. Cao, J. Song, L. Liu and Y. Yang, Influence of KOH followed by oxidation pretreatment on the electrochemical performance of phenolic based activated carbon fibers, *J. Electroanal. Chem.*, 2007, **611**(1–2), 225–231.

65 C. Lei, F. Markoulidis, Z. Ashitaka and C. Lekakou, Reduction of porous carbon/Al contact resistance for an electric double-layer capacitor (EDLC), *Electrochim. Acta*, 2013, **92**, 183–187.

66 M. He, K. Fic, E. Frąckowiak, P. Novák and E. J. Berg, Ageing phenomena in high-voltage aqueous supercapacitors investigated by in situ gas analysis, *Energy Environ. Sci.*, 2016, **9**, 623–633.

67 M. Biswal, A. Banerjee, M. Deo and S. Ogale, From dead leaves to high energy density supercapacitors, *Energy Environ. Sci.*, 2013, **6**, 1249–1259.

68 Q. Li, Y. Q. Zhu and S. J. Eichhorn, Structural supercapacitors using a solid resin electrolyte with carbonized electrospun cellulose/carbon nanotube electrodes, *J. Mater. Sci.*, 2018, **53**, 14598–14607.

69 J. Noh, C. M. Yoon, Y. K. Kim and J. Jang, High performance asymmetric supercapacitor twisted from carbon fiber/MnO_2 and carbon fiber/MoO_3, *Carbon*, 2017, **116**, 470–478.